Materials Research Bulletin 49 (2014) 237–244

Contents lists available at ScienceDirect

Materials Research Bulletin

journal homepage: www.elsevier.com/locate/matresbu

Synthesis of Fe/SiO_2 and iron oxides/SiO_2 nanocomposites by long-term ball milling

G. Pozo López [a,b,*], A.M. Condó [c,d], S.E. Urreta [a], S.P. Silvetti [a,b]

[a] Facultad de Matemática, Astronomía y Física, Universidad Nacional de Córdoba, Ciudad Universitaria, 5000 Córdoba, Argentina
[b] Instituto de Física Enrique Gaviola – CONICET, Argentina
[c] Centro Atómico Bariloche, Comisión Nacional de Energía Atómica – Instituto Balseiro, Universidad Nacional de Cuyo, Av. Bustillo 9500, 8400 San Carlos de Bariloche, Argentina
[d] Consejo Nacional de Investigaciones Científicas y Técnicas (CONICET), Argentina

ARTICLE INFO

Article history:
Received 6 June 2013
Received in revised form 27 August 2013
Accepted 1 September 2013
Available online 8 September 2013

Keywords:
A. Composites
A. Magnetic materials
A. Nanostructures
C. Electron microscopy
C. X-ray diffraction

ABSTRACT

Iron oxide/SiO_2 nanocomposites are synthesized by dry ball-milling a mixture of *bcc* Fe and α-quartz powders for prolonged times. A sequence of nanocomposites is obtained, with small magnetic particles dispersed in a non magnetic, amorphous matrix. The powders are characterized by X-ray diffraction and transmission electron microscopy. The magnetic hysteresis properties are investigated in the range 50–300 K. After 120 h milling, deformed, non-spherical, α-Fe nanocrystallites of about 10 nm in size and very few small (<10 nm) maghemite particles are found. At room temperature, iron particles are ferromagnetic and a large effective magnetic anisotropy is estimated, which is mainly attributed to surface effects. Between 160 and 200 h milling, maghemite nanoparticles are observed while after 220 h grinding, hematite phase appears; after 340 h milling, the sample consists of ferromagnetic hematite particles with a broad size distribution (5–50 nm) embedded in an amorphous matrix.

1. Introduction

Magnetic nanocomposite materials based on iron and iron oxides dispersed in ceramic matrixes have attracted great interest mainly because of their many and broad applications [1]; these include data storage, magnetic resonance contrast-enhancing media, gas sensors, magnetic fluids, magnetic refrigeration, magneto-optics and bioprocessing, among others. Size effects become important in these nanoscale featured materials, giving rise to complex magnetic behaviours often requiring a different approach as compared to bulk materials [2,3]. The main features determining the magnetic behaviour of these composite systems are the particle size distribution, the large volume fraction of atoms in and nearby the surface, the eventual appearance of a superficial oxide layer and magnetic interactions, strongly dependent on the dispersion of magnetic particles into the non-magnetic host [4].

For Fe/SiO_2 nanocomposites, many authors report unexpectedly high room temperature coercivities, ranging from $\mu_0 H_C = 35$ mT to over 150 mT [4,5], as compared to the value predicted by the Stoner–Wohlfarth model assuming anisotropy values close to the bulk one. Another interesting property of Fe nanoparticles dispersed or embedded in different matrixes, is that they exhibit a strong uniaxial effective anisotropy, in spite of their cubic crystal symmetry [6,7]. Surface anisotropy due to broken symmetry or spin disorders at the particle surfaces is believed to play a dominant role in such fine particulate systems [8].

Nowadays, composites containing γ-Fe_2O_3 (maghemite) nanocrystals are also intensively investigated for their potential applications in magnetic-tape media, colour imaging, magnetic memories for computers, magneto-optical devices, bioprocessing, catalysis and ferrofluids. Maghemite is a ferrimagnetic material which represents the low temperature phase of iron oxide, and it easily transforms to the more stable phase, hematite (α-Fe_2O_3), when submitted to temperatures above 653 K [9–11]. The development of new synthesis routes for maghemite nanoparticles is still of great interest. The usual technique needs two steps: the synthesis of nanoparticles by coprecipitation in alkaline solution of ferrous and ferric cations and then, the particle oxidation by a treatment in air, at temperatures between 373 K and 523 K [12].

Different methods have been reported in the literature for preparing iron and iron oxide nanocomposites, such as wet chemical synthesis, sol–gel processing and sputtering. In recent years, high energy mechanical milling has been used as a versatile and non-expensive technique for producing non-equilibrium

* Corresponding author at: Facultad de Matemática, Astronomía y Física, Universidad Nacional de Córdoba, Ciudad Universitaria, 5000 Córdoba, Argentina. Tel.: +54 351 4334051; fax: +54 351 4334054.
E-mail address: gpozo@famaf.unc.edu.ar (G. Pozo López).

0025-5408/$ – see front matter © 2013 Elsevier Ltd. All rights reserved.
http://dx.doi.org/10.1016/j.materresbull.2013.09.003

phases in several ways, such as nanostructured and amorphous materials with a broad range of chemical compositions, nanocomposites and extended solid solutions [13,14]. This relatively simple synthesis technique, with only a few operation parameters, is suitable for large scale commercial production [15]. Maghemite nanoparticles and maghemite/silica nanocomposites have been already prepared by high energy mechanical alloying, using hematite (α-Fe_2O_3) [12] and chemistry-derived α-Fe_2O_3/SiO_2 gel powders [16] as precursors, and also from grinding iron powders in water [12].

In this paper we report the results obtained with an alternative route to produce iron/and iron oxide/SiO_2 composites. Two basic crystalline precursors, α-Fe and SiO_2 powders are dry milled in a medium energy planetary mill for long times, under air atmosphere. In this case, large amounts of energy are also supplied to the powder but at a low rate promoting the formation of different metastable phases. It was possible to sequentially obtain composites containing iron, maghemite and hematite nanoparticles dispersed in amorphous silica, directly from iron and quartz powders. The microstructure evolution, the different iron containing phases forming during milling and the magnetic hysteresis properties of the different composites are then described.

2. Experimental procedures

Analytical grade α-Fe (99.4% purity) and SiO_2 (99% purity) crystalline powders, were used as starting materials for ball milling. The milling was carried out in a Fritsch Pulverisette 5 planetary ball-mill equipped with hardened steel balls and vials. These precursor powders were first milled separately to reduce their particle size, until both had a similar mean crystallite size, of about 65 nm for α-Fe and 50 nm for quartz. Then, these pre-milled powders were mixed to achieve the proportion: 50 wt.% α-Fe + 50 wt.% SiO_2. The initial ball to powder mass ratio was 10:1 and the mixture was milled at a speed of 200 rpm, for times up to 340 h, in air atmosphere without any additive (dry milling). The milling process was interrupted after selected times to take out small amounts of powder for characterization. Samples were then labelled Sx, where x refers to the total milling time in hours.

Crystalline phases and the microstructure of the milled products were monitored by X-ray diffraction (XRD) and transmission electron microscopy (TEM) respectively. X-ray diffraction profiles were recorded by a Philips PW 3830 diffractometer, operated in Bragg–Brentano geometry, with Cu Kα radiation (λ = 1.5418 Å) in the $10^\circ \leq 2\theta \leq 100^\circ$ range. XRD results were used to determine the phases present in the powders and their lattice parameters and average crystallite sizes. The morphology of the nanocomposite powders was observed by a Philips CM200UT TEM operating at 200 kV. Samples for TEM observation were prepared by dispersing a small amount of the powders in ethanol and depositing a drop of each emulsion on a holey carbon-coated copper grid.

Samples for magnetic measurements were prepared by cold-pressing the as-milled powders under 5 tons pressure, into cylinders of 6.5 mm in diameter and typically 2 mm in height. The magnetic field was applied parallel to the sample diameter and the actual internal field was calculated as $\mu_0 H_i = \mu_0 H_a - N J$, with $\mu_0 H_a$ the applied field, N ($\cong$0.18) the demagnetizing factor and J the magnetic polarization. Room temperature hysteresis curves were recorded by a vibrating sample magnetometer (VSM) Lakeshore 7300, with a maximum field up to 1.5 T. The magnetization as a function of temperature was studied in a Quantum Design SQUID magnetometer, in the range between 5 K and 300 K, following the zero field cooling (ZFC) and field cooling (FC) protocols. The sample is first cooled from room temperature to 4 K, without any applied field and the ZFC curve is recorded during heating under an applied field of 10 mT. The FC curve is then measured during a second heating run, keeping the external field applied. In addition, isothermal hysteresis loops were traced in the same temperature range up to 1.5 T.

3. Results and discussion

3.1. Microstructures

Fig. 1 shows the XRD patterns of the powders after different milling times. Sample S0 only shows the precursor oxides characteristic lines (α-Fe (bcc) and α-quartz); after 120 h milling, these diffraction peaks become less intense and significantly broadened, as expected for a continuous reduction in particle/crystallite size and a progressive microstrain (defects) during the milling process. A new phase appears in sample S160, but due to the large structure distortions induced by milling, the identification by X-ray diffraction is not conclusive. This new phase is also found in sample S180, but as the crystalline structure of maghemite is almost identical to that of the inverse spinel magnetite [10,17] it could not be identified with this technique as magnetite (Fe_3O_4) nor maghemite (γ-Fe_2O_3).

This phase was further investigated by measuring the room temperature Mössbauer spectrum, in transmission geometry, using a constant acceleration spectrometer with a 10-mCi ^{57}CoRh source. Fig. 2 shows the results for samples S120, S160 and S180; points are experimental data and the thick continuous line is the fitting curve, obtained by the addition of the different contributions shown. The fitting parameters as the isomeric shift (δ) referred to the metallic iron, the quadrupole splitting (ΔQ), the hyperfine field (B) and the percentage (P) are listed in Table 1.

Sample S120 is the only one exhibiting a weak magnetic interaction at room temperature, evidenced by a sextet (Zeeman splitting). It also shows two paramagnetic signals while a doublet is not observed because of a fast superparamagnetic relaxation. The first paramagnetic interaction has an isomeric shift near that of Fe^{3+} while in the second one it is about that of Fe^{2+}. These interactions are likely to arise in mixed Fe and Si oxides. The parameters corresponding to the magnetic interaction are similar to those of metallic iron (α-Fe). No traces of magnetite are

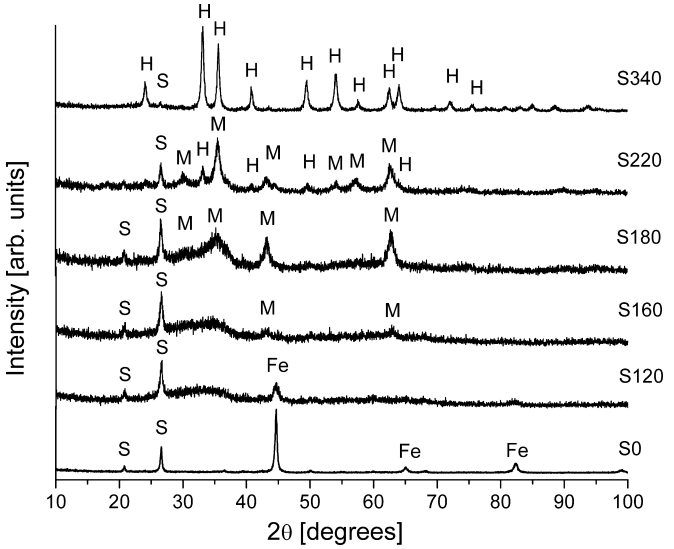

Fig. 1. X-ray diffraction patterns of samples Sx after different milling times. The principal diffraction lines of the α-Fe (Fe), α-quartz (S), maghemite (M) and hematite (H) are indicated.

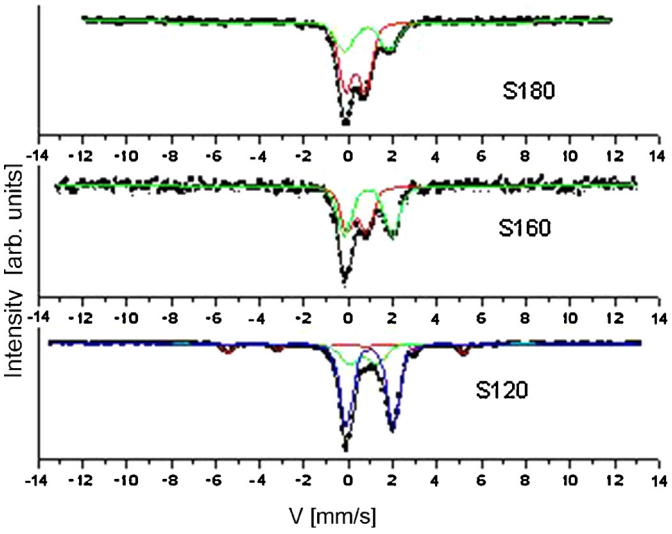

Fig. 2. Mössbauer spectra corresponding to samples S120, S160 and S180. The fitted parameters are listed in Table 1.

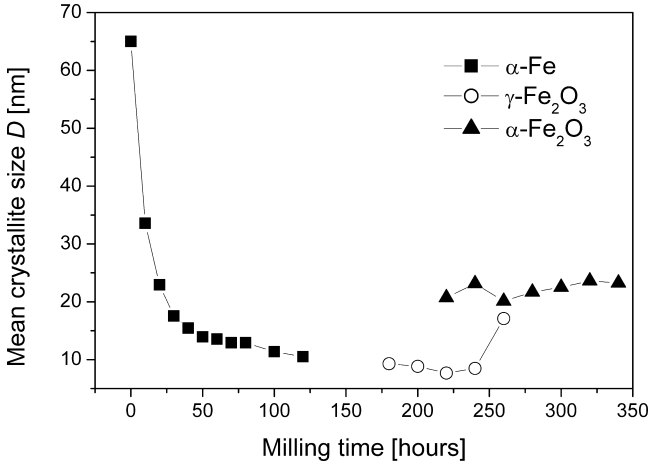

Fig. 3. Scherrer's mean crystallite size D of the major phases in the samples as a function of milling time.

observed indicating that the XRD peaks first observed in S160 and becoming more evident in sample S180 do not correspond to the magnetite phase.

At room temperature, the bulk γ-Fe_2O_3 (maghemite) phase has an isomeric shift of 0.35 mm/s referred to the mean value of sites A and B in the spinel structure. The isomeric shift observed in sample S160 is in agreement with the values reported in the literature, confirming the presence of maghemite in the nanocomposite. In sample S160 an incipient doublet is also detected, which relative intensity increases during milling. In sample S180 this doublet largely predominates in the spectrum indicating that as milling proceeds the fraction of particles undergoing superparamagnetic relaxation increases.

After 220 h milling, other new diffraction peaks appear, which are further enhanced in sample S340 and correspond to the hematite phase (α-Fe_2O_3). Between 220 and 340 h milling, the volume fraction of hematite increases at expenses of maghemite and at 340 h milling only the hematite diffraction lines are detected.

The average crystallite sizes D of the different phases present in the powders, monitored as a function of milling time, are shown in Fig. 3. The average crystallite size was estimated using the Scherrer equation [18]: $D = (0.9\lambda)/(\mathrm{FWHM}_i \cos\theta)$, where FWHM_i is the full width at half maximum (FWHM) after subtraction of the instrumental contribution, λ is the X-ray wavelength and θ is the Bragg angle. As can be seen in Fig. 3, the mean crystallite size of iron, D_{Fe}, gradually decreases from 65 nm, for sample S0, to 10 nm, in sample S120. The mean crystallite size of maghemite, determined after 180 h milling, is always lower than that of hematite, and it varies between 8 and 17 nm.

TEM observations were made on samples S120, S160, S180, S220 and S340 due to their particular phase characteristics. S120 is the last sample for which the α-Fe X-ray diffraction peaks could be measured while S160 is the sample where the maghemite diffraction lines begin to be detected. Samples S180 and S220 were chosen because of being the first ones in which the maghemite and hematite phases could be identified, respectively; sample S340, is the final product, and essentially consists of hematite particles dispersed in an amorphous silica matrix.

Fig. 4a is a typical dark field (DF) TEM image of sample S120, where *bcc* iron nanocrystallites (10 ± 4) nm in size, well dispersed in an amorphous matrix, can be observed. The selected area electron diffraction (SAED) pattern, presented in the inset, shows the α-Fe 110 ring and diffused rings corresponding to the amorphous matrix. High resolution images (HRTEM) were also taken; Fig. 4b shows a HRTEM image of one of these nanoparticles dispersed in the amorphous matrix. The (1 1 0) lattice planes of α-Fe (d_{110} = 2.027 Å) can be observed inside the particle, corresponding to the spots in the fast Fourier transform (FFT) shown in the inset. At this milling time, crystalline α-quartz particles are also observed, with a broad size distribution between 20 nm and 500 nm, in complete agreement with XRD results. But in this sample, another minor and quite small phase is found, as shown in the HRTEM image presented in Fig. 4c. Here, the (2 2 0) lattice planes of maghemite (d_{220} = 2.953 Å) can be observed in a 8 nm-size particle, indicating that maghemite phase is already present at this stage of milling.

Fig. 5a presents a dark field (DF) TEM image of sample S160, where nanosized maghemite particles, dispersed in an amorphous matrix are observed, together with crystalline quartz particles; the selected area diffraction pattern corresponding to the central zone of this image is shown in the inset. Here, well-dotted diffraction rings are observed, corresponding to the 4 0 0 and 4 4 0 reflections from maghemite, confirming the presence of many and very small particles of this phase: (8 ± 3) nm. Fig. 5b shows a HRTEM image of a maghemite particle embedded in the amorphous matrix. The Fourier transform of the particle, corresponding to the maghemite $[\bar{1}14]$ zone axis is shown in the inset.

TEM observations indicate that sample S180 consists of only maghemite nanoparticles of about (12 ± 4) nm dispersed in the amorphous matrix, in complete agreement with XRD results.

In the case of sample S220, DF TEM observations show maghemite, hematite and a few remaining quartz particles

Table 1
Mössbauer parameters: hyperfine field B, isomeric shift δ, quadrupole splitting ΔQ and percentage P in samples S120, S160 and S180.

Sample	B (Oe)	δ (mm/s)	P (%)	ΔQ (mm/s)	δ (mm/s)	P (%)	ΔQ (mm/s)	δ (mm/s)	P (%)
S120	330_1	0.01_1	6.4_6	1.22_7	0.78_2	23_2	2.11_1	1.07_1	71_3
S160	–	–		0.89_5	0.49_3	45_2	2.16_5	1.00_2	55_2
S180	–	–		0.85_2	0.421	64_1	1.98_4	0.95_2	36_1

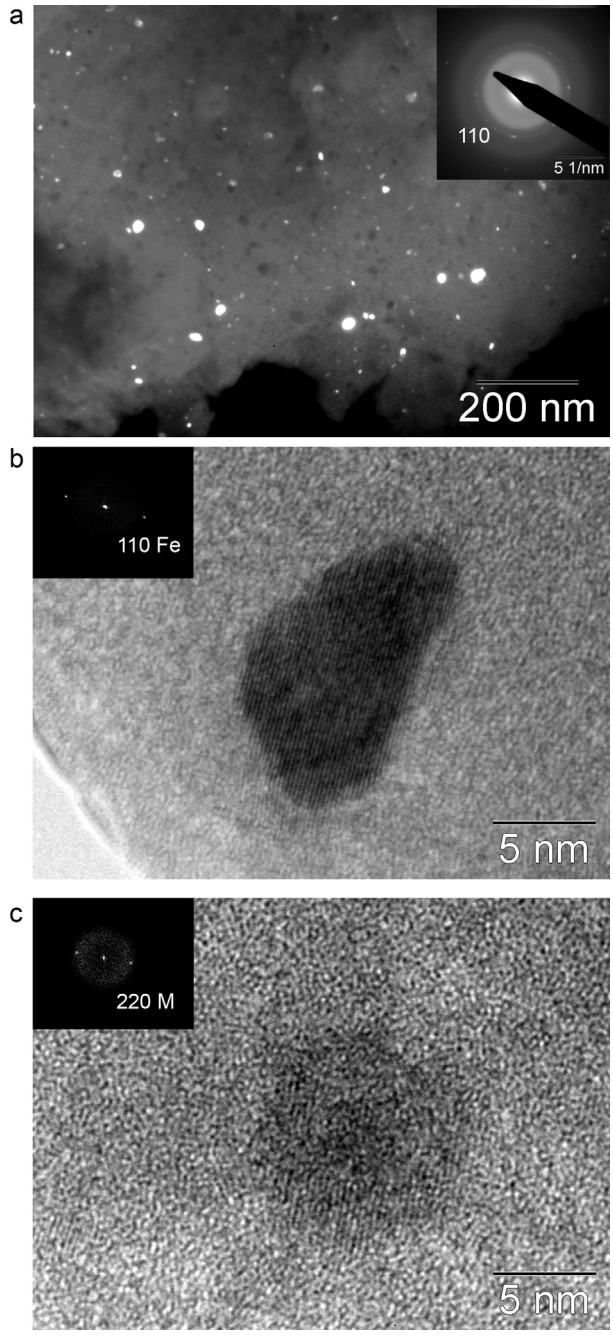

Fig. 4. (a) Dark field (DF) TEM image of sample S120, using the 1 1 0 ring from α-Fe, showing the α-Fe nanoparticles well-dispersed in an amorphous matrix. The corresponding selected area diffraction pattern is also presented in the inset. HRTEM images showing (b) α-Fe 1 1 0 lattice planes and (c) maghemite 2 2 0 lattice planes. This is clearly defined in the corresponding FFT inset.

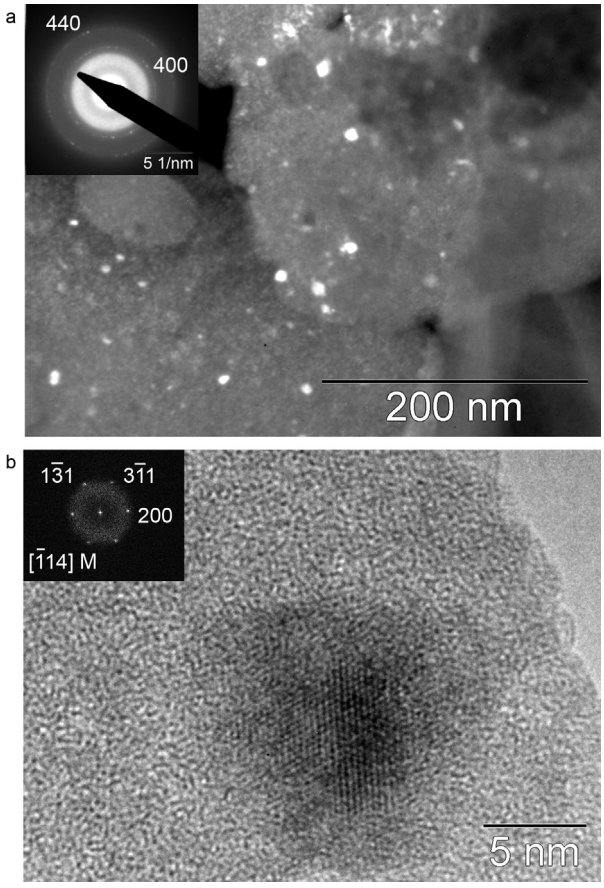

Fig. 5. (a) Dark field (DF) TEM image of sample S160 using the 4 4 0 reflection from maghemite. Nanosized maghemite particles dispersed in an amorphous matrix are observed together with quartz crystalline particles. The selected area diffraction pattern of the central region, showing the 4 0 0 and 4 4 0 diffraction rings from maghemite, is also shown in the inset. (b) HRTEM image of a maghemite crystalline particle embedded in the amorphous matrix. The inset shows the Fourier transform of the particle, corresponding to the maghemite $[\bar{1}14]$ zone axis.

dispersed in the amorphous matrix. Hematite particles have a mean particle size around (15 ± 6) nm and maghemite particles of about (13 ± 5) nm. Fig. 6a is a SAED pattern in which maghemite and hematite rings can be observed. Fig. 6b is a HRTEM image of a maghemite particle dispersed in the amorphous matrix with the corresponding FFT.

Finally, after 340 h milling, TEM images (Fig. 7a) show hematite particles with a broad size distribution, ranging from a few nanometers to about 50 nm, embedded in the amorphous silica matrix. A HRTEM image of the sample is shown in Fig. 7b together with the Fourier transform of the central particle (11 nm diameter) corresponding to the $[1\bar{1}1]$ zone axis of hematite.

At this point it is worth to note that the X-ray diffraction intensity profiles of maghemite particles formed during milling are considerably different from those reported for the standard XRD powder pattern for cubic maghemite, e.g. PDF #39-1346. These discrepancies are more notorious in samples S160 and S180, where the (4 0 0) and (4 4 0) diffraction lines are intensified, not only in the XRD patterns but also in the electron diffraction rings. It is a known fact that maghemite possesses the same inverse spinel structure as magnetite except for some cation vacancies occupying octahedral positions. Synthetic maghemite often displays superstructure peaks/spots, arising in cation and, therefore, vacancy ordering. It has been observed that the vacancies can be distributed: at random (space group $Fd\bar{3}m$), as the lithium cation in $LiFe_5O_8$ (space group $P4_132$) and with an ordered distribution with tetragonal symmetry (space group $P4_32_12$). The extent of vacancy ordering is related to the crystallite size, the precursor nature and the amount of Fe^{II} in the structure [19,20]. In our samples, the extra XRD reflections from the superlattice structure were not seen and the zone axes observed by TEM were properly identified considering a cubic symmetry, confirming the hypothesis that very small particles of maghemite do not show vacancy ordering [21]. So, the anomalies observed in the intensity distribution of some XRD peaks may arise in the differences in the cation distribution among the tetrahedral and octahedral sites in the spinel lattice. The higher intensity of the (4 0 0) and (4 4 0) reflections appearing in

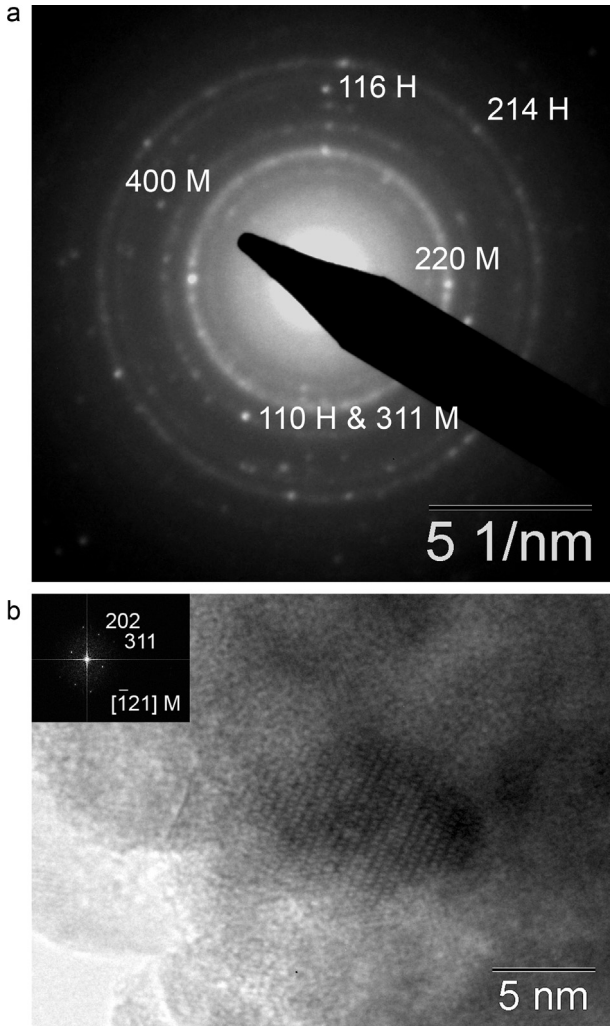

Fig. 6. (a) Selected area diffraction pattern of sample S220 showing maghemite (2 2 0), (3 1 1) and (4 0 0) rings and hematite (1 1 0), (1 1 6) and (2 1 4) rings. (b) HRTEM image of a maghemite crystalline particle embedded in the amorphous matrix and its Fourier transform corresponding to the maghemite $[\bar{1}21]$ zone axis.

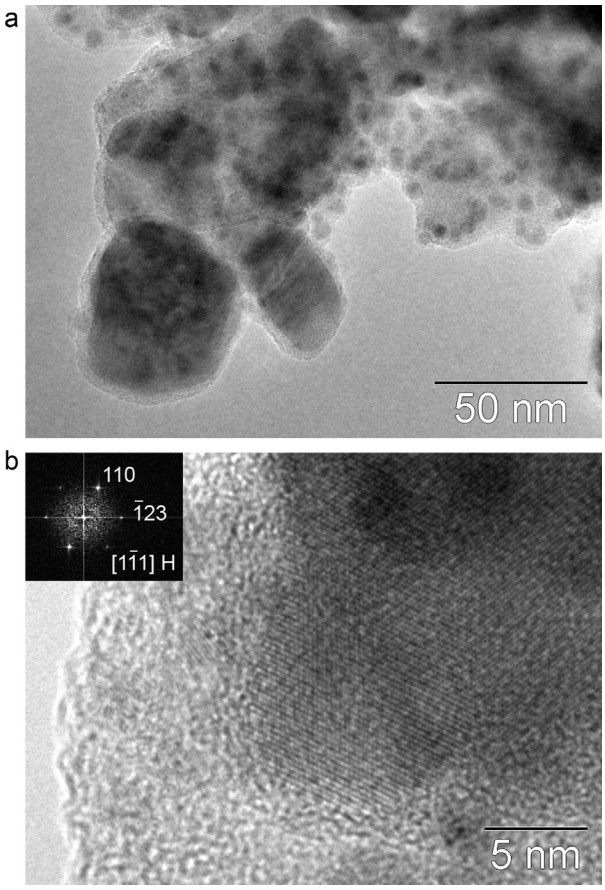

Fig. 7. (a) TEM bright field image showing the general morphology of sample S340 and (b) HRTEM image of a hematite crystalline particle embedded in amorphous silica matrix. Inset: Fourier transform of the particle, corresponding to the hematite $[1\bar{1}1]$ zone axis.

samples S160 and S180 would be then indicating a preferential octahedral cation occupancy during early stages of maghemite formation.

3.2. Room temperature magnetic properties

The evolution of room temperature magnetic properties (saturation magnetization, remanence and coercivity) during milling is summarized in Fig. 8. The saturation magnetization (M_S) gradually decreases with time up to 180 h milling, accompanying precursor's amorphization. Coercivity $\mu_0 H_C$, in this time interval, first grows until 60 h milling and then largely decays. This behaviour can be explained by considering that the magnetic phase in the powders is Fe-bcc, which continuously reduces its particle size during milling, as was shown in Fig. 3. So, the initial increase in coercivity is consistent with multi-domain iron particles with an increasing coercive force as the particle size decreases [22]. Sample S60 exhibits the highest coercivity value (55.4 mT) and represents the boundary between multi-domain and single-domain regimes. According to XRD analysis, this critical single-domain diameter should be around 14 nm, a value somewhat smaller than that reported for Fe, of about 25 nm [1]. The large coercivity value measured is also higher than those reported for similar Fe/SiO_2 nanocomposites synthesized by ball-milling (~35.0 [23], ~38.5 [3] and ~54.0 mT [24]).

The smallest coercivity value is found in sample S180 (6.2 mT); at this milling time M_S begins to rise due to the appearance of ferromagnetic maghemite. At 220 h milling, the weakly ferromagnetic hematite phase appears and magnetization monotonously decays up to 340 h milling, where it presents a minimum value (0.5 Am^2/kg). On the other hand, coercivity remains almost constant in the range 180–260 h of milling, taking values around

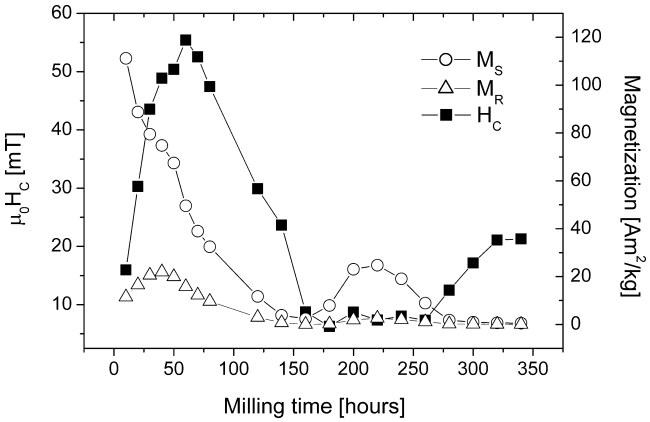

Fig. 8. Room temperature coercivity ($\mu_0 H_C$), remanence (M_R) and saturation (M_S) magnetization evolution with the milling time.

7 mT, and then increases again until 340 h milling, reaching a final value of 21.3 mT. The room temperature hysteresis curves of samples S120, S160, S180 and S220 are presented in Fig. 9.

3.3. Temperature dependence of magnetic properties

The temperature dependence of magnetization was explored in both, the zero field cooled (ZFC) and the field cooled (FC) conditions. These magnetization measurements provide an estimation of the mean blocking temperature of the particle ensemble and also of the magnetic particle size distribution [25] in the composite. In a typical ZFC–FC curve for a given particle ensemble, two characteristic temperatures can be distinguished: the mean blocking temperature T_B, defined as the temperature for which the ZFC curve presents its maximum value, and the irreversibility temperature T_{irr}, that is the temperature for which the ZFC and FC curves bifurcate. T_{irr} indicates the onset of blocking for the largest particles while T_B can be related to the blocking temperature of the average particle volume. Another important temperature is that at which the $d(M_{FC} - M_{ZFC})/dT$ versus T curve reaches a maximum. This curve is related to the activation barrier distribution; when the anisotropy energy is proportional to the particle volume, it is proportional to the size distribution profile [25]. Then, the corresponding blocking temperature distributions were obtained from the derivative $d(M_{FC} - M_{ZFC})/dT$ of the experimental data, as described in [25,26]. Fig. 10 displays the corresponding curves for samples S120, S160, S180 and S220.

ZFC–FC curves for sample S120 (Fig. 10a) indicate blocking temperatures above 300 K, suggesting a dominant ferromagnetic behaviour in the temperature range studied. As was previously mentioned, sample S120 mainly consists of α-Fe particles with an average grain size of about 10 nm, and small, spherical maghemite particles smaller than 8 nm. Besides their small size, the ensemble of iron particles behaves ferromagnetically, with a relatively high coercivity. A similar behaviour is observed by Kumar et al. [27]. These authors studied a system of α-Fe particles of about 9 nm in size embedded in an amorphous alumina matrix, presenting a ferromagnetic behaviour; they find superparamagnetism only for particles below 5 nm in size.

In these samples, the maghemite particles are then responsible for the blocking temperature distribution around 11 K and 26 K. Fitting the blocking temperature distribution to a log-normal one and considering the magnetic anisotropy constant for bulk maghemite (1×10^5 J/m^3) [20], these values of blocking temperatures result in mean particle sizes of about (5 ± 2) nm, in complete agreement with the maghemite particle sizes observed by TEM.

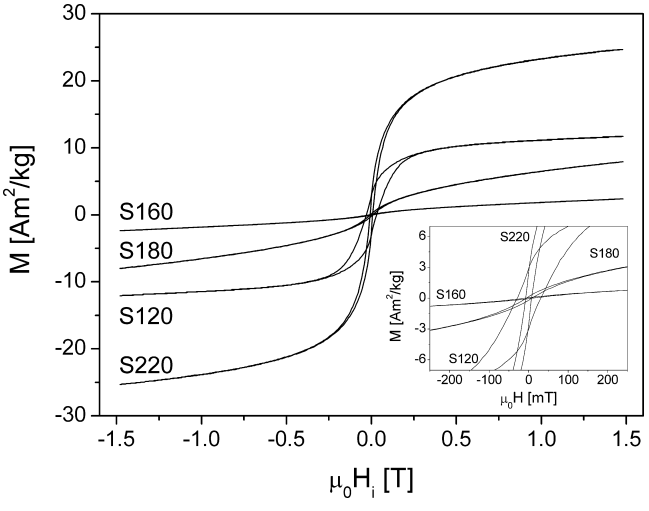

Fig. 9. Room temperature hysteresis loops of the samples milled for 120, 160, 180 and 220 h. The inset on the lower right corner displays remanence and coercivity.

Fig. 10b presents the ZFC–FC curves for sample S160, which show a well defined maximum for the M_{ZFC} curve at T_B = 58 K and an irreversibility temperature around 290 K. These features in the curves indicate the presence of a superparamagnetic contribution in the sample and the difference in the values of T_B and T_{irr} suggests a quite wide particle size distribution. Fitting a log-normal profile to the blocking temperature distribution, the mean maghemite particle size results (6 ± 1) nm, in fair coincidence with the mean value obtained by TEM observations (see Table 2).

For sample S180 (Fig. 10c) the M_{ZFC} curve maximum is at T_B = 109 K and the irreversibility temperature at around 300 K. Again, the difference between these temperatures indicates a broad particle size distribution and, since these temperatures have moved to higher values, an increase in the magnetic mean particle size is also expected. Fitting the blocking temperature distribution leads to a mean maghemite size of (8 ± 2) nm, in good agreement with the XRD and TEM sizes, as shown in Table 2.

In the case of sample S220 (Fig. 10d), the mean blocking temperature is about T_B = 225 K and the irreversibility temperature is above room temperature. Two phases coexist in this sample: small maghemite particles and larger hematite ones. Considering maghemite particles as responsible for the superparamagnetic behaviour observed, an average particle size of (8 ± 2) nm results, which is indistinguishable from the ones obtained from XRD and TEM studies.

Isothermal hysteresis curves of sample S120 were measured at different selected temperatures. The coercive field monotonously increases as the measuring temperature decreases from 300 to 50 K, as is observed in Fig. 11. Considering that the specimen is an ensemble of small particles of different magnetic phases, exhibiting a particle size distribution, the ferromagnetic contribution detected may be attributed to those particles having higher blocking temperatures, which are thermally more stable or to interparticle interactions, coupling the magnetic moments of close particles. If these interactions are disregarded, a simple model can be applied to describe the data in Fig. 11. The coercivity of a system of identical, non-interacting, single-domain particles with uniaxial anisotropy is expected to follow the relation [28,29]:

$$\mu_0 H_C(T) = \mu_0 H_C(0) - \frac{\mu_0 H_C(0)}{T_B^{1/2}} T^{1/2} \quad (1)$$

with $\mu_0 H_C(0)$, the effective anisotropy field, equal to $2K_{eff}/M_S$, where M_S is the saturation magnetization and K_{eff} is an effective anisotropy constant, with various contributions such as magnetocrystalline, shape or strain [30], T_B is the mean blocking temperature of the ferromagnetic particles and T is the absolute temperature. Then, fitting Eq. (1) to the $\mu_0 H_C$ vs. T curves leads to an effective anisotropy value K_{eff} and from the relationship $T_B = K_{eff} V/25k_B$ [22], the mean volume V of the particles determining coercivity may be estimated. As this analysis applies for a switching mechanism involving coherent magnetization rotation in each particle [29,31], it gives a good agreement with experimental data only for sample S120, for which $\langle T_B \rangle$ is well above room temperature, as illustrated by the ZFC–FC curves. Fig. 11 shows the plot $\mu_0 H$ vs. $T^{1/2}$ corresponding to sample S120 and the linear fit to data from which parameters were estimated. The resulting values are $\mu_0 H_C(0) = (97 \pm 1)$ mT, $\langle T_B \rangle = (430 \pm 10)$ K, $K_{eff} = (83 \pm 1) \times 10^3$ J/m^3 and $\langle d \rangle = (15 \pm 2)$ nm, in good agreement with a blocking temperature above 300 K resulting from the ZFC–FC curves (Fig. 10a) and the mean particle sizes obtained by TEM and XRD. These Fe particle sizes are comprised in the range 15–20 nm, for which the coherent rotation mode of magnetization

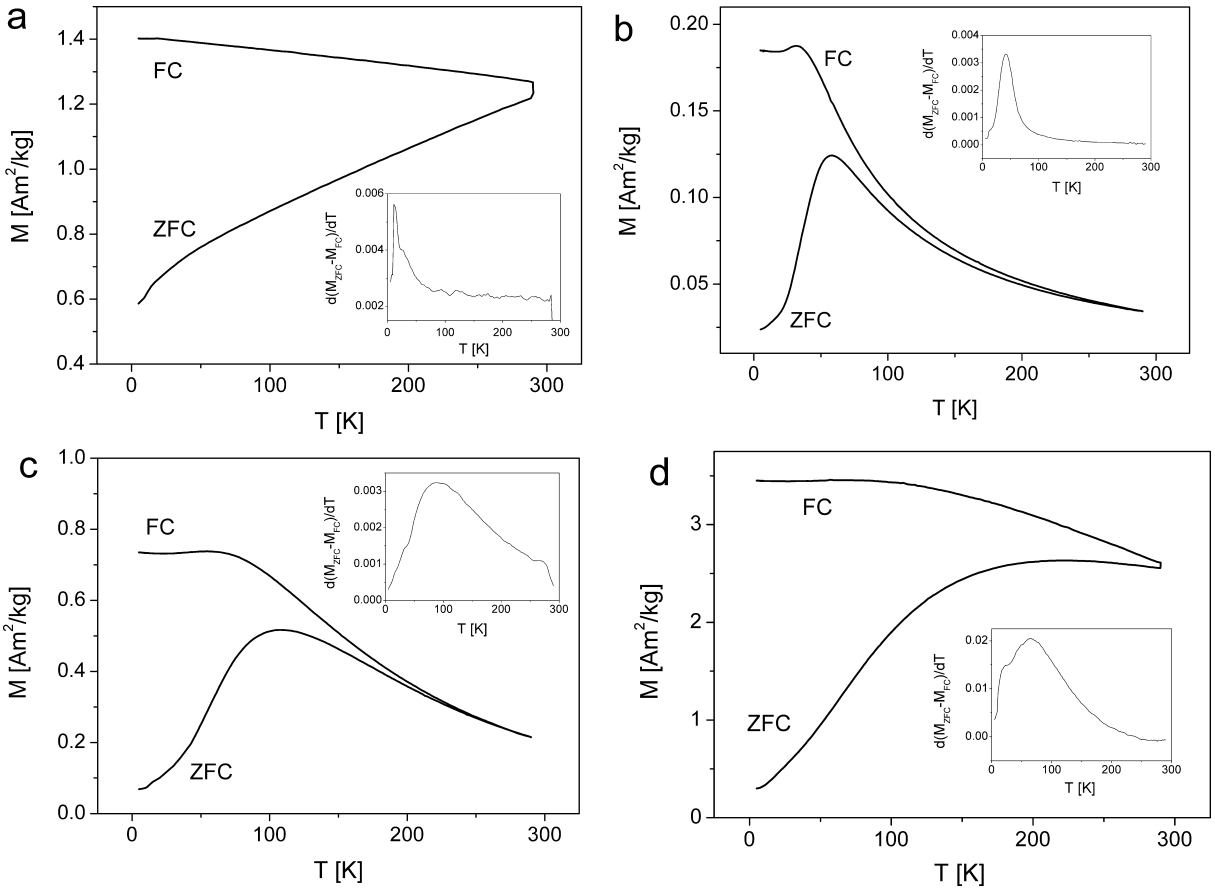

Fig. 10. ZFC and FC curves under an applied field of 10 mT for the samples milled (a) 120, (b) 160, (c) 180 and (d) 220 h. Also shown in the corresponding insets are the apparent blocking temperature distributions calculated from the ZFC and FC curves.

reversal is more favourable than the non-uniform curling and buckling modes [8,32].

The fitted value for the effective anisotropy constant is higher than that reported for bulk iron (48×10^3 J/m^3 [1]); in addition, in spite of the iron cubic crystal symmetry it exhibits an uniaxial character, evidenced by a M_R/M_S value near 0.5 at 5 K, in complete agreement with early published results on iron nanoparticles synthesized by other methods and embedded in different matrixes or supports [6–8,33–35]. Possible factors enhancing the particle anisotropy energy are the exchange anisotropy between metallic core and oxide shell (core–shell model), the magnetoelastically induced anisotropy due to large stress between a metal particle and the surrounding matrix, shape anisotropy due to deviation of particle shape from ideal sphere, and surface anisotropy due to broken symmetry or spin disorder at the particle surfaces. The first possibility cannot be responsible for the high effective anisotropy constant obtained, since HRTEM images do not show any iron oxide shell around the iron nanoparticles, neither a shift of the hysteresis loops at low temperatures due to exchange bias between antiferromagnetic hematite (α-Fe_2O_3) or wüstite (FeO) shells and the Fe cores [33,34]. Second, if each Fe particle is severely strained due to large misfit stresses between the particle and the surrounding matrix, magnetoelastic effects could give a possible explanation to the large coercive force observed, but following a very simple argument [7,36] the magnetoelastic energy is limited to the order of 10^3 J/m^3, and this energy is much smaller than the magnetocrystalline anisotropy energy. Moreover, comparing the lattice parameter for α-Fe with the one obtained from

Table 2
Average crystallite size D for the predominant phases in samples S120, S160, S180 and S220, obtained with XRD and TEM techniques.

Sample	D [nm]	D_{TEM} [nm]	Phase
S120	10 ± 8	10 ± 4	α-Fe
S160	–	8 ± 3	γ-Fe_2O_3
S180	9 ± 8	12 ± 4	γ-Fe_2O_3
S220	8 ± 8	13 ± 5	γ-Fe_2O_3
	21 ± 8	15 ± 6	α-Fe_2O_3

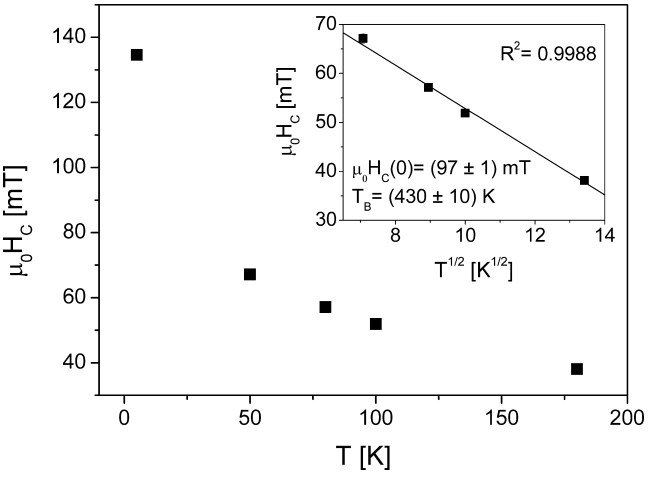

Fig. 11. Temperature dependence of the coercive field $\mu_0 H_C$ for sample S120. The inset shows $\mu_0 H_C(T)$ to obey a $(T)^{1/2}$ dependence for this sample.

XRD results, it is found that the Fe (1 1 0) lattice spacing distortion is below 0.2%, indicating that the iron particles are not so seriously strained. Another possible factor is a shape effect. According to HRTEM images the iron particles in sample S120 can be considered as prolate ellipsoids elongated in z direction, so that the magnetic shape anisotropy can be written as $K_{shape} = \mu_0 M_S^2 (N_{x,y} - N_z)/2$, where $N_{x,y}$ and N_z are the demagnetization factors along the short- and long-axis directions, respectively [7,28,33]. From this formula and considering that the ratio of long axis to short axis is about 1.8 in our particles, the shape magnetic anisotropy can be estimated around 4×10^3 J/m^3, which is one order of magnitude smaller than the anisotropy constant of bulk Fe.

Some other authors have speculated that surface anisotropy is the principal responsible for the enhancement in the effective anisotropy of fine particles. Following the quite simple model of a linear relationship between K_{eff} and $1/d$ presented by Bødker et al. [6], the parameters of that linear fit were used for a particle of about d = 10 nm and the effective anisotropy constant encountered ($K_{eff\ \ Bødker} = (84 \pm 48) \times 10^3$ J/m^3) resulted indistinguishable from the one obtained in this work from the fitting of the H_C vs. $T^{1/2}$ curve ($(83 \pm 1) \times 10^3$ J/m^3). So, the high effective magnetic anisotropy energy found for the iron nanoparticles in sample S120 is likely to be due to surface effects. However, an influence of interactions on the apparent anisotropy cannot be completely excluded.

4. Conclusion

Bcc Fe and α-quartz are dry ball-milled for prolonged times and different nanocomposites are obtained as milling proceeds. After 120 h milling, deformed, non-spherical α-Fe nanocrystallites, 10 nm in size, are found dispersed in the amorphous silica matrix. Besides their size, these iron particles are ferromagnetic in the temperature range studied and they reverse their magnetization by a coherent rotation mechanism; the large effective magnetic anisotropy found is explained on the basis of surface effects.

Samples grinded between 160 and 220 h consist of superparamagnetic maghemite nanoparticles (8–13 nm) embedded in amorphous silica.

Beyond 220 h milling, hematite phase appears and its volume fraction increases at expenses of maghemite. The ferromagnetic contribution to the hysteresis loop observed may be attributed to hematite (about 20 nm) while the superparamagnetic contribution is likely to arise in small remaining maghemite particles. After 340 h milling, the sample mainly consists of hematite particles embedded in amorphous silica.

Acknowledgments

The authors wish to thank SECyT-UNC and CONICET for the financial support given for the realization of this work. The authors also thank Dr. A.F. Cabrera (Departamento de Física, Facultad de Ciencias Exactas, Universidad Nacional de la Plata) for Mössbauer measurements.

References

[1] R.C. O'Handley, Modern Magnetic Materials, Principles and Applications, John Wiley and Sons, 2000.
[2] J.L. Dormann, D. Fiorani (Eds.), Magnetic Properties of Fine Particles, North-Holland, Amsterdam, 1992.
[3] G.C. Hadjipanayis, G.A. Prinz (Eds.), Science and Technology of Nanostructured Magnetic Materials, Plenum Press, New York, 1991.
[4] M. Alonso-Sañudo, J.J. Blackwell, K. O'Grady, J.M. González, F. Cebollada, M.P. Morales, J. Magn. Magn. Mater. 221 (2000) 207.
[5] J.J. Blackwell, M.P. Morales, K. O'Grady, J.M. González, F. Cebollada, M. Alonso-Sañudo, J. Magn. Magn. Mater. 242–245 (2002) 1103.
[6] F. Bødker, S. Mørup, S. Linderoth, Phys. Rev. Lett. 72 (2) (1994) 282.
[7] C. Chen, O. Kitakami, Y. Shimada, J. Appl. Phys. 84 (4) (1998) 2184.
[8] T. Ibusuki, S. Kojima, O. Kitakami, Y. Shimada, IEEE Trans. Magn. 37 (4) (2001) 2223.
[9] R.Y. Hong, H.P. Fu, G.Q. Di, Y. Zheng, D.G. Wei, Mater. Chem. Phys. 108 (2008) 132.
[10] S. Solinas, G. Piccaluga, M.P. Morales, C.J. Serna, Acta Mater. 49 (2001) 2805.
[11] D. Ortega, J.S. Garitaonandia, C. Barrera-Solano, M. Ramírez-del-Solar, E. Blanco, M. Domínguez, J. Non-Cryst. Solids 352 (2006) 2801.
[12] R. Janot, D. Guérard, J. Alloy Compd. 333 (2002) 302.
[13] J.Z. Jiang, Y.X. Zhou, S. Mørup, C. Bender Koch, Nanostruct. Mater. 7 (1996) 401.
[14] A. Kihal, B. Bouzabata, G. Fillion, D. Fruchart, Phys. Procedia 2 (2009) 665.
[15] T. Tsuzuki, F. Schaffel, M. Muroi, P.G. McCormick, J. Alloy Compd. 509 (2011) 5420.
[16] J.M. Xue, Z.H. Zhou, J. Wang, Mater. Chem. Phys. 75 (2002) 81.
[17] N. Randrianantoandro, A.M. Mercier, M. Hervieu, J.M. Grenèche, Mater. Lett. 47 (2001) 150.
[18] H. Klug, L. Alexander, X-ray Diffraction Procedures for Polycrystalline and Amorphous Materials, 2nd ed., John Wiley and Sons, New York, 1974.
[19] M.P. Morales, C. Pecharroman, T. Gonzalez Carreño, C.J. Serna, J. Solid State Chem. 108 (1994) 158.
[20] R.M. Cornell, U. Schwertmann, The Iron Oxides. Structure, Properties, Reactions, Occurences and Uses, 2nd edition., Wiley-VCH Verlag GmbH & Co., KGaA, Weinheim, 2003.
[21] R. Grau-Crespo, A.Y. Al-Baitai, I. Saadoune, N.H. De Leeuw, J. Phys.: Condens. Matter 22 (2010) 255401.
[22] B.D. Cullity, Introduction to Magnetic Materials, Addison-Wesley, Reading, MA, 1972.
[23] J. Hu, Y. Wang, K. Wang, B. Hu, F. Yang, N. Tang, H. Pan, Y. Zhou, Z. Wang, Solid State Commun. 95 (11) (1995) 771.
[24] A.K. Giri, C. de Julián, J.M. González, J. Appl. Phys. 76 (1994) 6573.
[25] M. Knobel, W.C. Nunes, L.M. Socolovsky, E. De Biasi, J.M. Vargas, J.C. Denardin, J. Nanosci. Nanotechnol. 8 (2008) 2836.
[26] M. Knobel, L.M. Socolovsky, J.M. Vargas, Rev. Mex. Fis. E 50 (2004) 8.
[27] D. Kumar, J. Narayan, A.V. Kvit, A.K. Sharma, J. Sankar, J. Magn. Magn. Mater. 232 (2001) 161.
[28] G. Bertotti, Hysteresis in Magnetism, Academic Press, Inc., San Diego, 1998.
[29] E.F. Kneller, F.E. Luborsky, J. Appl. Phys. 34 (3) (1963) 656.
[30] A.H. Morrish, The Physical Principles of Magnetism, IEEE Press, New York, 2001 .
[31] E.C. Stoner, E.P. Wohlfarth, Philos. Trans. R. Soc. London, Ser. A 240 (1948) 599.
[32] G. Xiao, C.L. Chien, Appl. Phys. Lett. 51 (16) (1987) 1280.
[33] D.-L. Hou, X.-F. Nie, H.-L. Luo, J. Magn. Magn. Mater. 188 (1998) 169.
[34] J. Carvell, E. Ayieta, A. Gavrin, R. Cheng, V.R. Shah, P. Sokol, J. Appl. Phys. 107 (2010) 103913.
[35] L.-M. Lacroix, S. Lachaize, A. Falqui, T. Blon, J. Carrey, M. Respaud, J. Appl. Phys. 103 (2008) 07D521.
[36] S. Chikazumi, Physics of Ferromagnetism, Clarendon, Oxford, 1997.